Materials Science Forum
ISSN: 1662-9752, Vol. 1185, pp 111-125
doi:10.4028/p-1wZ1l6

Submitted: 2026-01-19
Revised: 2026-02-16
Accepted: 2026-02-24
Online: 2026-04-15

Experimental and Numerical Study of Steel-Aluminium Rotary Friction Welding with Heat Flux via Subroutine

MATHEW Amith Tom[1,a*], PIWEK Armin[1,b], MAJER Jakub[2,c], MOHNFELD Norman[1,d], BEHRENS Bernd-Arno[1,e] and UHE Johanna[1,f]

[1]Leibniz University Hannover, Institute of Forming Technology and Machines, An der Universität 2, 30823 Garbsen, Germany

[2]Poznań Institute of Technology, Łukasiewicz Research Network, Ewarysta Estkowskiego St. 6, 61-755 Poznań, Poland

[a*]mathew@ifum.uni-hannover.de, [b]piwek@ifum.uni-hannover.de, [c]jakub.majer@pit.lukasiewicz.gov.pl, [d]mohnfeld@ifum.uni-hannover.de, [e]behrens@ifum.uni-hannover.de, [f]uhe@ifum.uni-hannover.de (*corresponding author)

Keywords: Rotary friction welding, FEM, Tailored forming

Abstract. Rotary friction welding (RFW) is a solid-state process used to join similar and dissimilar materials, such as steel and aluminium. In RFW, interface temperature development and its distribution are essential factors influencing material bonding. It governs bond strength, the formation of intermetallic phases (IMPs) and the evolution of the heat-affected zone (HAZ). Thus, precise prediction of temperature distribution is vital for the reliable design and optimization of the RFW process, as well as for the prediction and control of IMP formation. This work presents an experimental investigation of the thermo-mechanical behaviour of EN AW-6082 and 20MnCr5 during RFW in addition to a corresponding novel numerical modelling framework. A systematic parameter study was conducted to evaluate the influence of the friction pressure, friction time, forging pressure, forging time and rotational speed on the peak temperature, sledge path and flash formation. In-situ temperature measurements were performed using thermocouples (TC) embedded in the steel component, while axial force, displacement and rotational speed were recorded. The results demonstrate that, within the investigated parameter ranges, the rotational speed is the dominant factor governing frictional heat generation and the peak temperature, while the friction pressure primarily influences the sledge path. In parallel, a 2D axisymmetric finite-element model with a user-defined subroutine was developed to compute the heat flux based on process parameters and contact conditions, providing a transparent and extensible numerical framework for RFW. The experimental findings establish a robust basis for the calibration and future validation of the numerical model.

Introduction

The automobile industry aims to reduce CO_2 emissions and thereby improving the energy efficiency by focusing on lightweight automobiles [1,2]. However, every component cannot be replaced by lightweight materials like aluminium. Critical structural components require materials that can withstand high temperatures and mechanical loads [1,3]. Tailored forming techniques are being developed to produce semi-finished hybrid parts which can fulfil these requirements [3,4]. Automotive manufacturing commonly employs both steel and aluminium alloys, either as individual materials or in hybrid component combinations. In particular, the development of steel-aluminium hybrid components has gained increasing attention due to their ability to combine high strength with weight reduction. This interest has motivated extensive research into suitable joining technologies, especially solid-state processes such as friction welding [5]. They are particularly favoured due to their cost-effectiveness and favourable mechanical properties. RFW technique is a plausible method of material joining especially when it comes to dissimilar material combinations [3,4].

Welding processes can be classified into fusion welding and solid-state welding, based on whether the base material is melted or not. In solid-state welding, heat is generated in the joining zone by external mechanical loading, whereas in fusion welding the joining zone is heated by an external heat

source [6]. RFW is a solid-state joining technique widely applied in aerospace, automotive and energy sectors for producing high-integrity joints with limited distortion [7]. In RFW, heat is generated through the conversion of mechanical energy into thermal energy at the interface between the rotating and axially loaded components. One component is rotated under axial pressure against a stationary counterpart and the resulting frictional heat rapidly raises the interface temperature, leading to localised material softening [7].

The RFW process is generally divided into two main stages: the friction phase and the forging phase [3,7]. The rotational speed is initially maintained at a constant value during the friction phase, while a predefined friction pressure is applied to generate heat at the interface. At the end of the friction phase, the spindle rotation is abruptly stopped and the axial force is increased to the forging pressure. This forging phase promotes material consolidation and joint formation promoting metallurgical bonding. Flash formation around the joint region demonstrates that significant plastic deformation and material expulsion occurs during the forging phase [7]. Given its advantages over conventional methods, including reduced costs, shorter welding times, higher accuracy, excellent bond strength resulting from its fine-grained structure, fewer welding defects and suitability for joining dissimilar materials, this technique offers significant benefits [8].

The rotational speed, friction time, friction pressure and forging pressure are important parameters that can be used to control the secondary parameters like friction heat and material flow, influencing the joint strength and weld quality [3]. At elevated rotational speeds and higher friction pressures combined with extended friction times, the heat generated at the interface increases, leading to a more uniform temperature distribution across the joining zone. However, the central region typically exhibits lower temperatures due to its lower relative velocity, resulting in reduced frictional heat generation near the axis of rotation [9]. Excessive heating under these conditions can promote pronounced thermal softening and grain coarsening in the weld zone, which has been linked to a deterioration of mechanical properties, including reduced joint strength. In contrast, more moderate combinations of rotational speed, friction pressure and friction duration produce lower peak temperatures and avoid excessive softening, thereby establishing a more stable process window in which higher joint strengths have been observed [10,11]. The large differences in thermal conductivity, flow stress and plastic deformation behaviour between steel and aluminium make thermo-mechanical control difficult during RFW. These mismatches strongly influence heat generation, flash formation, HAZ evolution and critically, the IMP formation at the interface [8,12]. Although the aluminium alloy remains below its melting temperature throughout the RFW process, diffusion mechanisms are activated, leading to the development of a layer consisting of intermetallic phases [3]. Although thin IMP layers can contribute to metallurgical bonding, excessive growth leads to extreme brittleness, impaired ductility and reduced fatigue performance [3,13]. IMP thickness and morphology are strongly governed by the thermal cycle generated during the friction and the axial pressure during the forging stages of RFW. Predicting the temperature evolution during friction welding is crucial, as the thermal field directly controls material flow and microstructural changes. The accurate prediction and control of heat generation are thus central to predicting and minimising intermetallic formation and ensuring joint integrity [3,12,13]. Since the key thermal quantities cannot be measured directly with standard machine sensors, process simulation provides essential insight into the transient temperature distribution within the joining zone [10].

Thermo-mechanical numerical modelling is particularly valuable for RFW processes because the welding occurs over short durations, involves highly coupled thermal and mechanical phenomena and is sensitive to process parameters [8,14]. Finite-element (FE) simulations provide a practical and cost-effective approach to quantify the thermo-mechanical behaviour, including temperature distribution, plastic strain, contact pressures and heat generation at the interface that are difficult to measure experimentally. Consequently, such simulations facilitate a deeper understanding of the underlying process physics and allow systematic optimization of welding parameters to improve joint quality and mechanical performance [14,15].

Numerical modelling of RFW used prescribed radial heat fluxes and rotational-speed dependencies, which revealed steep thermal gradients near the interface [16]. However, these early thermal models lacked mechanical coupling and neglected friction and contact physics. Their inability to predict flash formation and residual stresses further constrained their use for dissimilar material combinations [14]. The seminal 2.5D work of Moal & Massoni introduced axisymmetric FE models that retained circumferential kinematics. These models used adaptive remeshing to enable the predictive simulation of the rotational deceleration and sledge path during the welding of similar material combinations. However, the approach did not consider post-weld cooling, or interfacial phase changes and the experimental calibration was limited [17]. Davé et al. developed analytical thermal models for dissimilar welds where energy input was taken from measured angular speed curves and used to compute thermal profiles [18]. Later, Wang et al. and Lee et al. measured angular/torque histories to define interface thermal boundaries for coupled FE models [11,18]. D'Alvise et al. implemented a coupled thermo-mechanical RFW module with a pressure–speed–temperature friction law and validated it for similar and dissimilar nickel-based alloys. Although the model reproduced general parameter sensitivities, it systematically over-predicted weld time, forging and interface temperatures compared with experiments across weld conditions. This highlights the challenges in accurately modelling interface behaviour, particularly for dissimilar materials with strong thermal–mechanical contrasts [19]. Despite these advances, most studies remain focused on similar metal systems. Bennett's integrated FE study that explicitly included phase transformations and validated residual stress predictions represents a mature template for modern coupled RFW simulations. However, the investigation was restricted to monomaterial welding conditions involving steel [14]. Recent work by the authors on C22.8–41Cr4 friction welds employed the inbuilt Simufact friction welding module to develop a substitute thermo-mechanical model. However, the predictive capability of this approach decreased noticeably when process parameters were varied, with significant deviations observed during validation. More critically, the model relies on a simplified scaling factor, (described as the Y-Factor) in the frictional heat generation and energy-partitioning formulation [8]. Currently, there are insufficient detailed experimental data for dissimilar material combinations, particularly steel-aluminium joints, to reliably calibrate and validate predictive thermo-mechanical models. Therefore, experiments are required to investigate temperature evolution, thermal gradients and heat generation behaviour in these joints, as well as to provide insights into material flow and their dependence on process parameters. The data obtained from these experiments will form the foundation for developing accurate coupled models capable of capturing intermetallic formation in dissimilar metal systems.

To address this limitation, a fully physics-based 2D axisymmetric FE model was developed using a user-defined subroutine, providing explicit access to the interface friction laws, heat generation and material response. The development, calibration and validation of the numerical model require reliable experimental input, including accurate material data and experimental measurements acquired under representative process conditions. Therefore, RFW experiments were conducted using 20MnCr5 steel and EN AW-6082 aluminium alloy workpieces under various process parameter combinations (PCs). In-situ temperature measurements were performed during the welding process to capture the thermal evolution near the joint interface. A systematic parameter study was carried out based on the resulting experimental dataset to analyse the influence of key process parameters on the thermal and mechanical response of the joint. In order to evaluate the developed subroutine, the numerically calculated temperature curves were compared with the experimental curves.

Methods – Material Data

Comprehensive material data for EN AW-6082 and 20MnCr5, including temperature-dependent mechanical and thermal properties, have been previously investigated and reported in the prior studies from the same research framework [20]. The experimentally determined flow curves were used for the current numerical model. The flow behaviour was obtained from the isothermal compression tests conducted in the temperature range of 20-550 °C for EN AW-6082 and up to 1200 °C for 20MnCr5 at strain rates of 1, 10 and 50 s^{-1}[21]. The flow curves were then implemented in the numerical

material model using the Hensel–Spittel approach to describe the material response within the relevant thermo-mechanical regime of the RFW process. Eq. 1 describes the flow stress k_f as a function of plastic strain ε, temperature T and strain rate $\dot{\varepsilon}$. The material specific model coefficients as defined by Wester et al. is shown in the Table 1 [21].

$$k_f = Ae^{m_1 * T} T^{m_8} \varepsilon^{m_2} e^{\left(\frac{m_4}{\varepsilon} + m_6 * \varepsilon\right)} (1+\varepsilon)^{m_5 T} \dot{\varepsilon}^{(m_3 + m_7 T)} \quad (1)$$

Table 1. Material specific Hensel Spittel model coefficients [21]

Material	A	m_1	m_2	m_3	m_4	m_5	m_6	m_7	m_8
20MnCr5	3.08e-8	-0.0114	0.2787	-0.0973	-0.00053	-0.00024	-0.9644	0.00036	4.8115
EN AW-6082	1972.85	-0.0111	0.0197	-0.1779	-0.00158	0.00243	-0.7941	0.00087	0.1357

Methods – Experimental Investigation

The experimental study was carried out on a Genius Plus rotary friction welding machine from KUKA. Cylindrical specimens with a diameter of 40 mm and a length of 100 mm were used. The aluminium was positioned on the spindle (rotating) side, while the steel was mounted on the sledge (axially driven) side, Fig. 1(a), (b). Due to the significantly lower flow stress of aluminium, plastic deformation during friction welding occurred only in the aluminium component. Consequently, flash formation was confined to the aluminium specimen, while the steel remained essentially undeformed [22]. For this reason, temperature measurements were conducted exclusively in the steel specimen, where TC placement could be achieved without disturbing the material flow.

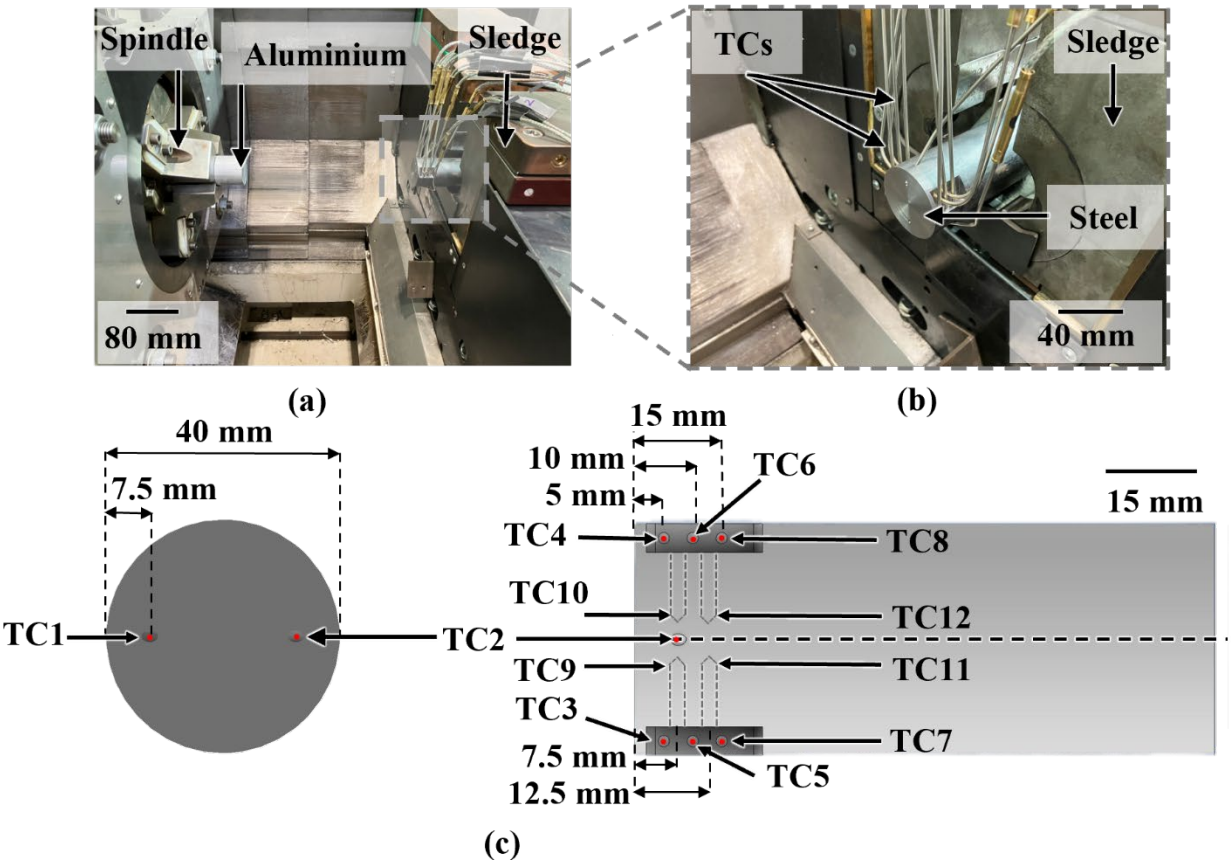

Fig. 1. (a) Configuration and positioning of the steel and aluminium specimens during the welding process; (b) steel specimen with TCs prior to welding and (c) schematic illustration of TC positions with annotations.

Temperature evolution was recorded at 12 locations using K-type TC with a diameter of 2 mm. TC were arranged symmetrically, with even-numbered TCs located on one side of the specimen and odd-numbered TCs on the mirrored side providing six mirrored measurement positions to improve accuracy and repeatability. TC1 and TC2 were placed at the friction interface and inserted through holes oriented at 45° to the specimen axis in order to capture the interface temperature. The remaining 10 TCs were positioned along the axial direction at distances as shown in Fig. 1(c). These TCs were arranged symmetrically on both sides of the specimen. The specimen was machined according to the schematic shown in Fig. 1(c) to accommodate the TCs and to ensure consistent sensor positioning across all experiments.

Experiments were designed considering 5 welding parameters as independent variables including friction pressure, friction time, forging pressure, forging time and rotational speed, while the resulting temperature curves as the dependent variable. The experimental design, consisting of 15 PCs is shown in Table 2. The PCs were defined based on prior work by Dewidar et al., where the effect of parameters on the mechanical properties were investigated [22]. The current work extends these PCs by incorporating multiple rotational speeds and by limiting the friction time in accordance with machine constrains. This approach enables future comparison of the results and supports the extension of the process.

Table 2. The experimental design consisting of 15 PCs, with values in brackets representing force in kN

Parameter combination	Friction pressure in MPa	Friction time in s	Forging pressure in MPa	Forging time in s	Rotational speed in rpm
1	80 (100.5 kN)	0.5	175 (220 kN)	5	700
2	119.4 (150 kN)	0.5	175	10	700
3	80	0.8	175	10	700
4	119.4	0.8	175	5	700
5	80	0.5	225 (282.7 kN)	10	700
6	119.4	0.5	225	5	700
7	80	0.8	225	5	700
8	119.4	0.8	225	10	700
9	80	0.5	225	10	1,400
10	80	0.5	225	10	1,750
11	80	0.5	225	10	2,100
12	119.4	0.5	225	10	700
13	119.4	0.5	225	10	1,400
14	119.4	0.5	225	10	1,750
15	119.4	0.5	225	10	2,100

In addition to the in-situ temperature measurements, the axial force, displacement and rotational speed were recorded from the machine and can be used to define the mechanical and kinematic input parameters for the numerical model. Fig. 2(a) shows the recorded evolution of key process parameters for PC1 during the RFW cycle. For this experiment, the rotational speed was maintained at 700 rpm and a friction force of 100.5 kN was applied during the friction phase. At the end of this phase, the spindle rotation was stopped and the axial force was increased to 220 kN for the forging phase. Fig. 2(b) presents the resulting welded specimen with aluminium flash around the joint. The RFW tests were repeated two times for each PCs. Specimens from the PCs 5, 9, 10 and 11 were separated along the longitudinal axis by wire erosion to compare the flash geometries.

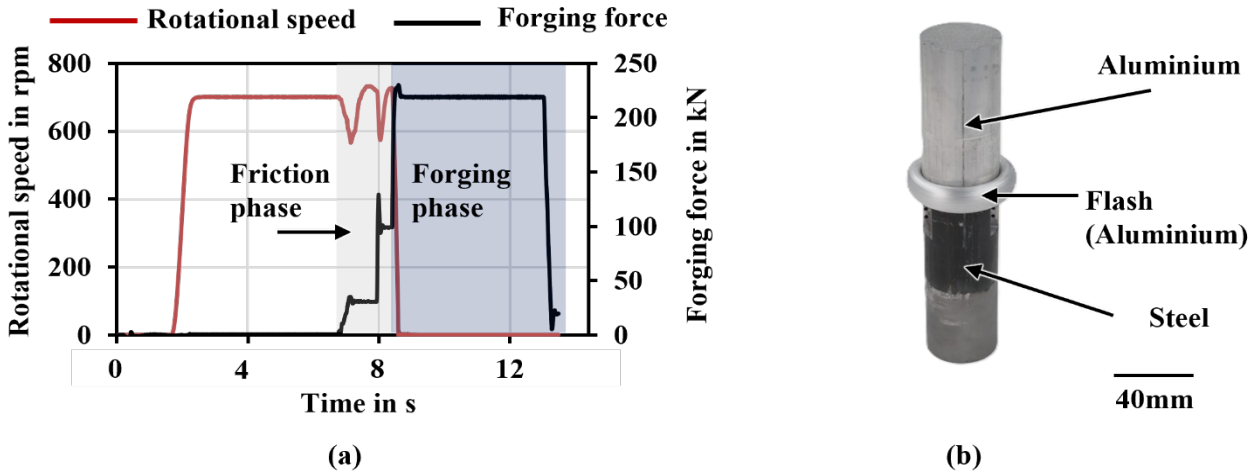

Fig. 2. (a) Schematic evolution of the main process parameters of PC1, illustrating axial force–time and rotational speed–time relationships; (b) final friction-welded specimen after completion of the process.

Numerical Modelling

A 2D axisymmetric model was developed in the simulation software Simufact.forming v16 for the numerical analysis. The model consists of two cylinders, aligned coaxially along the same axis, as illustrated in Fig. 3. Material models were assigned to the workpieces according to the experimental arrangement. The body with the material model for aluminium was assigned as the workpiece and the steel as a deformable die. The upper, lower and support dies were defined as rigid bodies. A spring was used to substitute the axial force during the friction and the forging phase. The spring force was applied between the ground and the upper die making the upper die movable in the Z-direction.

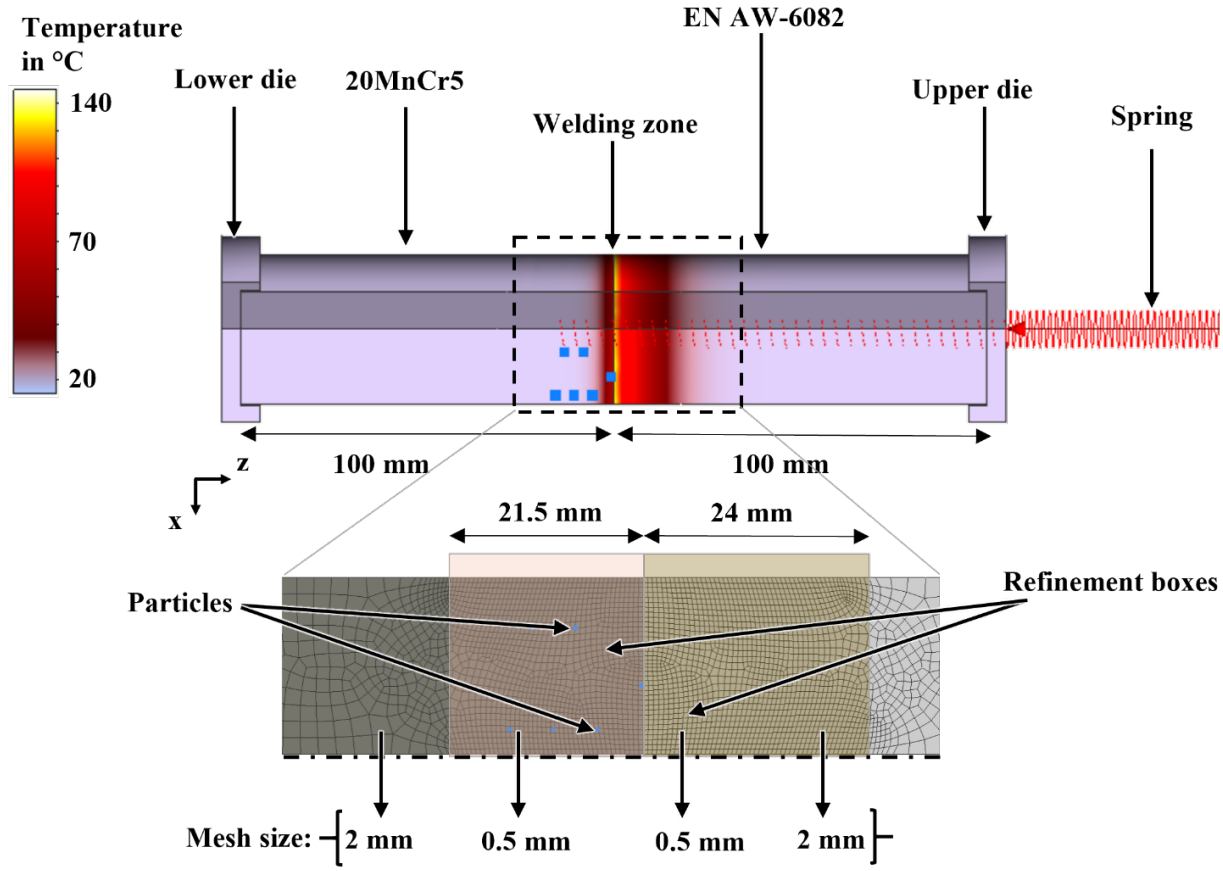

Fig. 3. Schematic representation of numerical model set up for 2D axisymmetric RFW simulation.

The combined friction model with a friction coefficient μ = 0.05 and a friction factor m = 0.05 was employed to describe the contact conditions between the two workpieces. These values were chosen based on preliminary simulations to match the experimental flow behaviour of the aluminium. This allows the model to capture the initial onset of material flow in aluminium without overestimating the interfacial resistance. These values can be further calibrated once the feasibility of the modelling approach is validated. In the simulation, particles were added to the same positions as the TCs on the steel workpiece to allow a direct comparison to the experiments. The model was set up in the cold forming/upsetting module in Simufact.forming. The geometries were discretised using elements of type Quads (10). To ensure that the numerical results are independent of the selected element size, a mesh dependency study was performed with global element sizes ranging from 3 mm to 0.5 mm. The computational time increased exponentially with the increasing mesh refinement as shown in Fig. 4(a). The average value of peak temperatures per increment during the friction phase in aluminium was evaluated for the different mesh sizes. The results showed that the predicted temperatures decreased with mesh refinement and stabilised at element sizes of 1 mm and 0.5 mm, which produced nearly identical results as in Fig. 4(b). A similar trend was observed for the average temperatures during the initial 2 seconds of the forging phase in the steel specimen, see Fig. 4(c). Considering the localized deformation at the joining interface, both the workpieces steel and aluminium were meshed with a global element size of 2 mm, with local mesh refinement applied at the weld interface to achieve an element size of 0.5 mm in this critical region, see Fig. 3. The required computational time and average temperatures when using the refinement box (RB) are also shown within the shaded regions in Fig. 4. Thus, a balance between computational efficiency and the accuracy in capturing the dominant thermo-mechanical trends of the process, consistent with the proof-of-concept nature of this study was acquired.

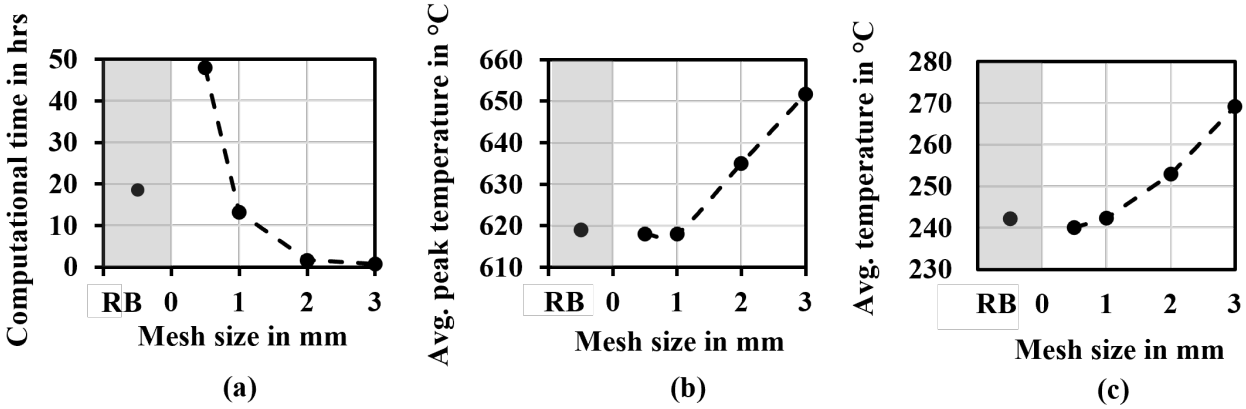

Fig. 4. Results of mesh study representing (a) computation time as function of mesh size; (b) evolution of peak temperatures in aluminium during the friction phase; (c) average temperatures in steel during the initial 2 seconds of the forging phase.

The existing friction welding module within the Simufact.forming v16 has its limitations as stated in [8]. Therefore, a user-defined subroutine structure was implemented in Simufact.forming to account for contact-dependent thermal loading at the material interfaces. The application of heat flux using the subroutine substitutes the heat energy produced due to rotation enabling the 2D simulation and significantly reducing computational cost and time. The implementation relies on a coordinated use of built-in user subroutine hooks executed at different stages of the solution procedure.

Fig. 5 represents a flowchart showing the subroutine calls in the Simufact. The subroutine UELOOP, which is called at every increment and iterates over all elements, was used to access the contact state information of the nodes of each element. For each increment, the contact identifiers (specifically contact touched body ID) associated with the nodes of the active elements were extracted and stored in nodal state variables. This approach allows the contact status of each node to be tracked throughout the simulation. In a subsequent step, the subroutine FORCDT, which is executed at every increment for a user-defined subset of nodes, was employed to apply thermal boundary conditions.

The subset of nodes evaluated by FORCDT was selected based on the corresponding body ID, thereby restricting the thermal calculations to the relevant material body. Nodes on which the frictional heat is to be applied were further identified and separated according to their specific contact identifiers.

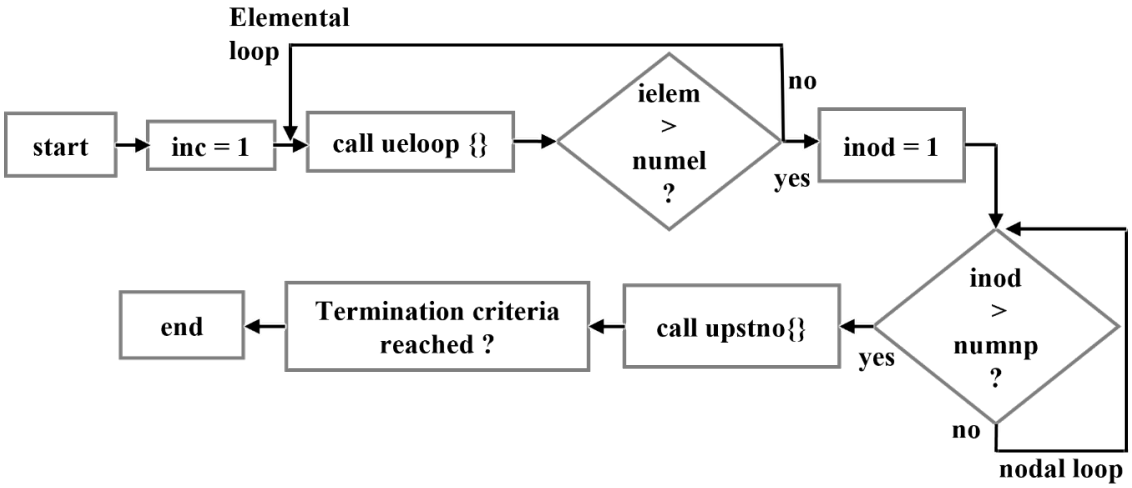

Fig. 5. Schematic representation of subroutine call in Simufact. Abbreviations: inc = increment, ielem = element number, numel = number of elements, inod = node number, nump = number of nodes.

The frictional heat flux q, was then calculated following the approach described by Lei et al. [23] as stated in Eq. 2, where η is the mechanical efficiency factor (set to 0.9), τ_f is the interfacial friction shear stress and v is the friction velocity defined as the product of angular velocity ω and radius r.

$$q = \eta \tau_f v \tag{2}$$

The interfacial friction shear stress was further modelled using the combined friction model given by Eq. 3, where μ is the coefficient of friction, p is the normal pressure at the integration points of the interface elements, m is the friction factor and σ_f is the flow stress. The term μp represents the Coulomb friction model and the term $m\frac{\sigma_f}{\sqrt{3}}$ corresponds to the shear friction model. The μ and m values were provided as 0.05 to be consistent with the mechanical model. Taking the minimum of these two terms prevents the Coulomb friction stress from rising unrealistically with increasing normal pressure [23].

$$\tau_f = min\,(\mu p, m\frac{\sigma_f}{\sqrt{3}}) \tag{3}$$

The previously stored nodal state variables were accessed within the FORCDT to calculate and apply the heat flux to the interface nodes. In this way, the thermal loading was applied exclusively at the material interfaces where contact was detected. To verify the correct identification of contact nodes and the consistent application of the heat flux, the stored nodal state variables were visualized using the UPSTNO subroutine. This post-processing step enables direct monitoring of contact conditions and the correct execution of the user-defined logic throughout the simulation.

Results and Discussion

Fig. 6(a) presents exemplary the temperature histories recorded at all TC locations for PC10. This demonstrates the similarity between symmetrically positioned measurement points. It can be seen that the temperatures along the symmetrical counterpoints are in agreement confirming the assumption of rotational symmetry during the process. In RFW, the temperature is highest at the

contact surface, as measured by TC1 and TC2 and decreases progressively with increasing axial distance from the interface (TC3–TC12). The frictional heat causes a rapid plastic flow of the aluminium and in combination with the superimposed pressure, the aluminium can enter the channels of TC1 und TC2. This pushes the TCs back, meaning they no longer measure the temperature directly at the interface. As a result, temperature measurements obtained at these near-interface locations tend to exhibit higher variability and reduced reliability compared to the other TCs as shown in Fig. 6(b). The recorded near-interface measurements thus showed a higher failure rate during the experiments. The measuring points further away from the interface showed stable and reproducible measurement results, as the measuring position could be maintained throughout the entire test. Intermediate points were used to capture the axial temperature gradient, providing additional information for understanding the thermal field. Therefore, datasets TC4, TC10, TC6, TC12 and TC8 in the order of increasing distance from the weld interface respectively were used for the parameter study.

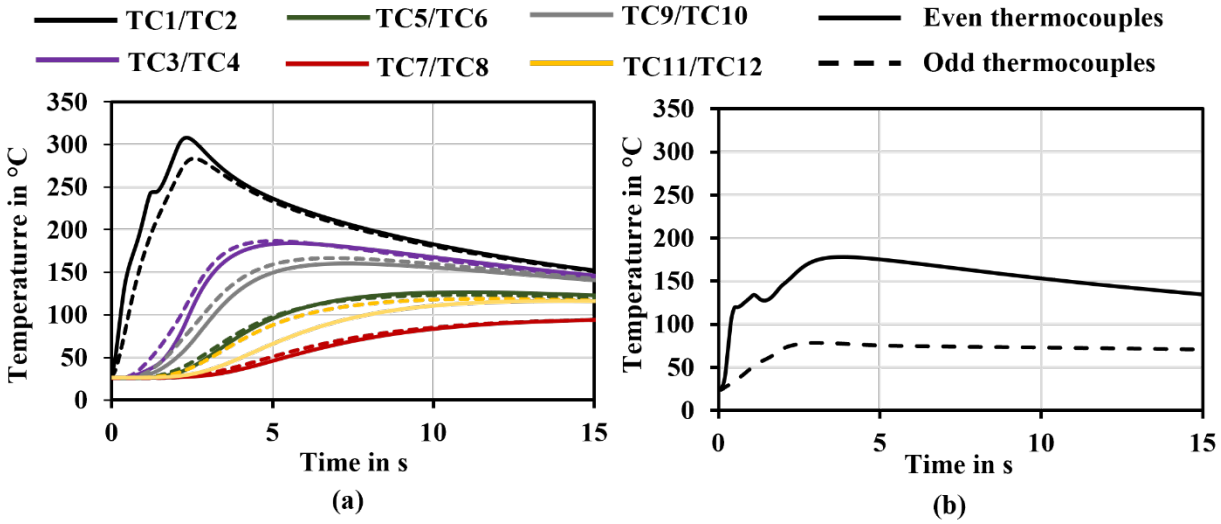

Fig. 6. (a) Temperature histories measured at the twelve TC locations for PC10; (b) TC1 and TC2 showing deviating behaviour in PC15 caused by flash formation and local mechanical disturbances near the weld interface.

The influence of RFW parameters on the peak temperature was evaluated using ANOVA and main effects analysis based on TC10. Although it is the second closest to the weld interface, TC10 provided reliable and reproducible measurements across all parameter combinations, making it the most representative of the thermal conditions governing joint formation. Fig. 7(a-e) presents the main effects plot for peak temperature at TC10, showing the adjusted mean temperature as a function of friction time, friction pressure, forging time, forging pressure and rotational speed. Friction time shows a strong positive effect on the peak temperature. An increase in friction time leads to a pronounced rise in the measured peak temperature. This behaviour is expected in RFW, as a longer friction phase increases the duration of interfacial sliding, thereby enhancing frictional heat generation and heat accumulation near the weld interface [10,11]. Friction pressure exhibits a relatively weak influence on the peak temperature at TC10. Increasing the friction pressure results in only a marginal increase in peak temperature. This indicates that, within the investigated range, friction pressure has a minor role in heat generation compared to other parameters. Forging time has minimal influence on the peak temperature. The main effects plot shows nearly identical mean temperatures for both levels of forging time, suggesting that peak temperature is largely established during the friction phase rather than the forging phase. Forging pressure demonstrates a moderate inverse effect on peak temperature. Increasing forging pressure slightly reduces the peak temperature. This reduction can be attributed to the enhanced plastic deformation and material expulsion during the forging phase, which promotes heat dissipation away from the interface. Rotational speed exhibits the strongest influence on peak temperature among all investigated parameters. A substantial increase in peak temperature is observed as rotational speed increases from the lowest to the highest level.

This trend reflects the direct relationship between rotational speed and frictional power input, as higher speeds significantly increase the rate of heat generation at the interface.

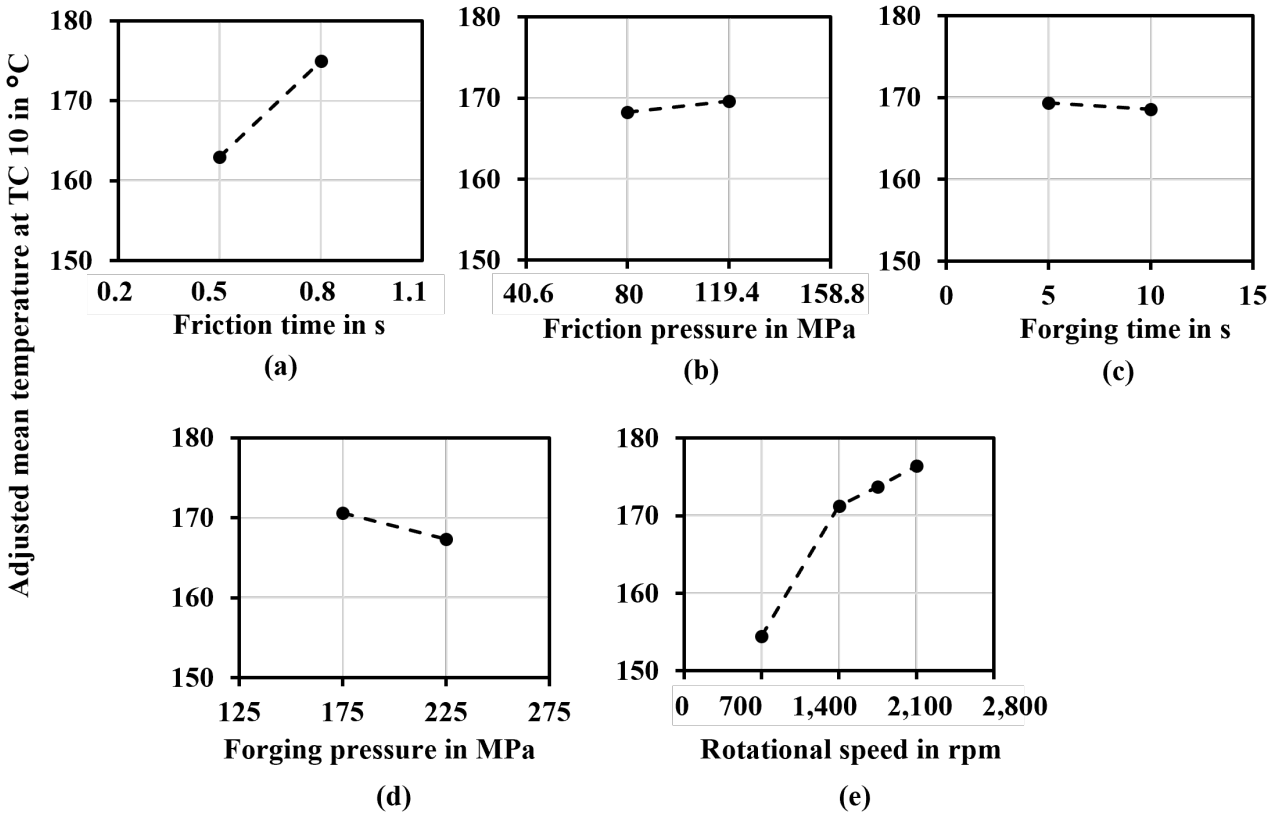

Fig. 7. ANOVA main effects plots for peak temperature at TC10 as a function of the process parameters a) friction time, b) friction pressure, c) forging time, d) forging pressure and e) rotational speed.

To further isolate the influence of rotational speed, four PCs namely, 5, 9, 10 and 11 with identical process conditions and with increasing rotational speeds were grouped as Set 1 and compared. This enables a focused evaluation of the effect of rotational speed on peak temperature measured by the five TCs TC4, TC10, TC6, TC12 and TC8 positioned at progressively increasing distances from the weld interface respectively**.** Fig. 8(a-e) illustrates the variation of peak temperature with rotational speed for the TCs. For all locations, an overall increase in peak temperature with increasing rotational speed was observed. The results clearly demonstrate that the rotational speed influences peak temperature at all measured locations, but the effect diminishes with increasing distance from the weld interface (TC4 > TC10 > TC6 > TC12 > TC8). The strong temperature response at TC4 and TC10 further emphasizes the importance of rotational speed control for regulating the thermal conditions, which are critical for joint integrity in dissimilar material RFW. The temperature drop observed at 2,100 rpm on TC4 falls within the experimental scatter due to the slipping out of TCs during the experiment.

The axial displacement of the sledge during the friction phase provides a quantitative measure of flash formation, as it directly reflects the plastic flow of aluminium driven by frictional softening at the interface. Measuring the sledge path in this stage allows the extent of material flow to be related to the frictional heat input, enabling assessment of how process parameters influence flash formation. Displacement data were exported from the machine and plotted as in Fig. 8(f) to examine trends with respect to rotational speed and friction pressure. Two sets of PCS were selected for the analysis. Set 1 consisted of the PC 5, 9, 10 and 11, all conducted at the lowest friction pressure of 80 MPa. Set 2 includes the PC 12, 13, 14 and 15, which employed the same sequence of rotational speeds but at the highest friction pressure of 119.4 MPa.

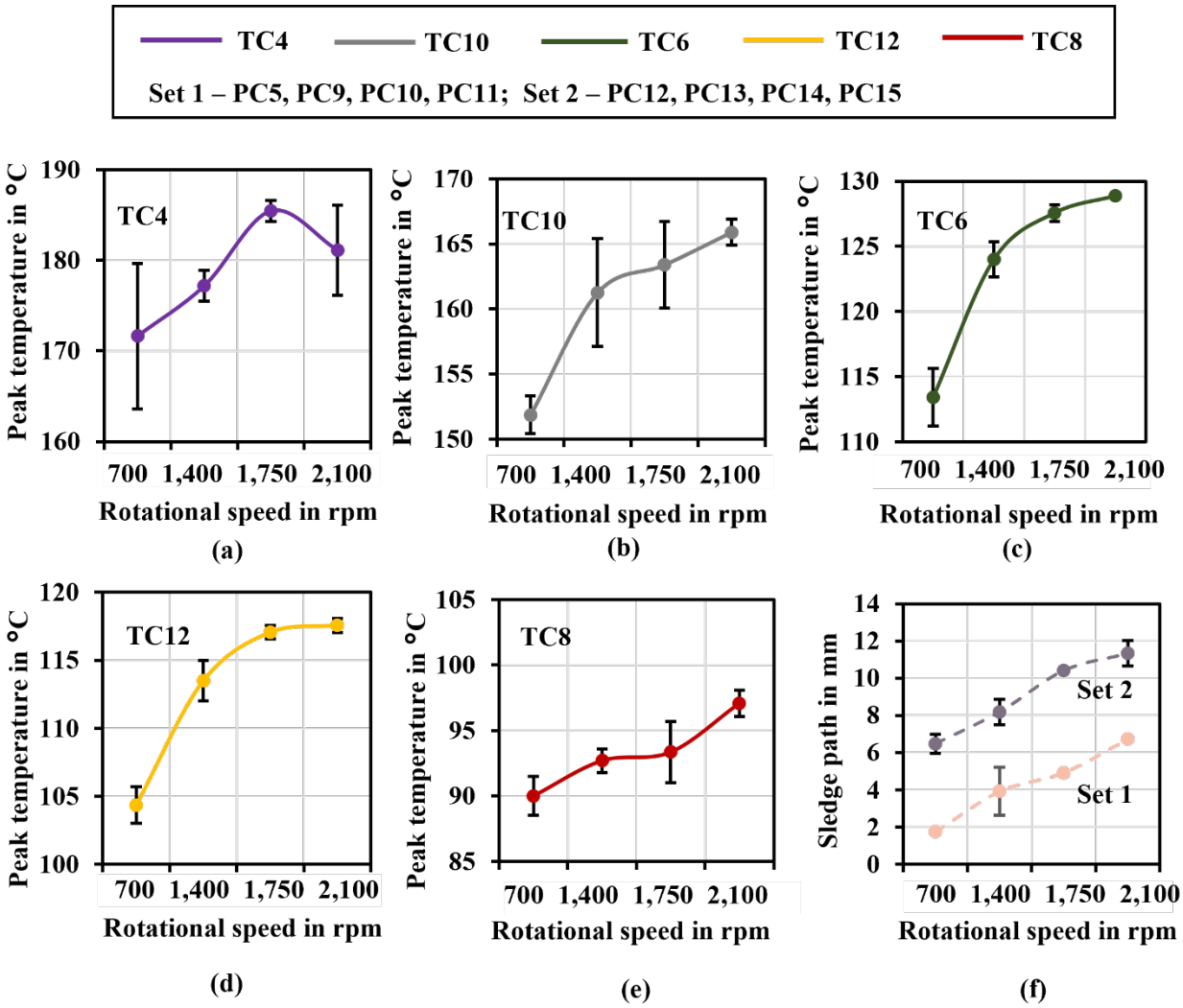

Fig. 8. (a-e) Peak temperature variation with rotational speed for TC4, TC10, TC6, TC12 and TC8; (f) axial displacement of the steel component during the initial friction phase for Set 1 (friction pressure 80 MPa) and Set 2 (friction pressure 119.4 MPa).

Fig. 8(f) presents the sledge path towards the aluminium counterpart during the initial friction phase. For both friction pressure levels, the sledge path increases with increasing rotational speed, indicating enhanced material softening and plastic flow due to higher frictional heat generation at elevated speeds. For example, in Set 1, increasing the rotational speed from 700 to 1,400 rpm approximately doubles the sledge path, from 1.74 mm to 3.91 mm, while a further increase to 2,100 rpm results in a sledge path of 6.73 mm. At a certain rotational speed, the sledge path is consistently greater at higher friction pressure. With increasing friction pressure more aluminium is pushed out of the joining zone at lower temperatures and the associated higher flow stresses. Even when similar interface temperatures are reached at the same friction time, higher friction pressure promotes greater material extrusion, leading to an increased sledge path and flash formation. Fig. 9 illustrates the evolution of flash geometry with increasing rotational speed. A progressive increase in flash size is observed at higher rotational speeds, which correlates well with the increased sledge path recorded by the machine data during the friction phase. This agreement confirms the enhanced plastic flow at elevated rotational speeds. Further, the cross-sectional images show the penetrated aluminium into the drilled holes for TC1 and TC2, which caused the TCs to be pushed out of their original positions.

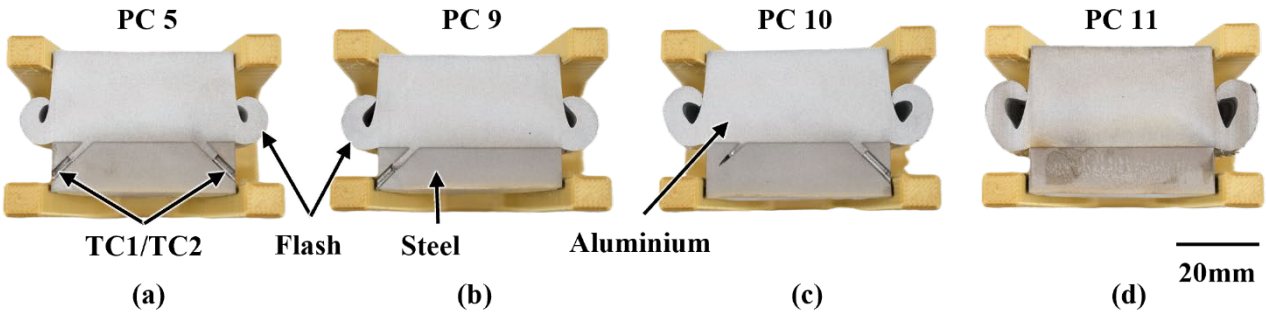

Fig. 9. Wire eroded specimens of set 1 showing the effect of rotational speed on flash formation with (a) 700 rpm, (b) 1,400rpm, (c) 1,750 rpm and (d) 2,100 rpm (lowest friction pressure 80 MPa).

Rotational speed is the primary driver of interface temperature, as evidenced by the ANOVA results and the corresponding increase in sledge path with increasing speed. The enhanced thermal softening at higher rotational speeds leads to greater plastic flow during the friction phase. In contrast, the axial pressure exhibits a limited influence on peak temperature within the investigated range but plays a significant role in governing mechanical deformation. Excessive axial pressure can force softened material out of the joining zone resulting higher sledge path and flash formation. As temperature decreases away from the interface, material from the HAZ may be incorporated into the weld, potentially reducing bonding quality and compromising the integrity of the joining interface. Consequently, while rotational speed governs thermal input, axial pressure primarily modulates the extent of plastic upset and must be carefully balanced to optimise joint strength.

To evaluate the numerical model, Fig. 10 shows a comparison of the simulated results with the experimental measurement of PC11. In Fig. 10(a) the temperature histories at locations where post particles were added in the simulation corresponding to the positions of the embedded TCs in the steel specimen are compared. The numerical model qualitatively captures the overall temperature evolution at all measurement locations, including the rapid temperature rise during the friction phase, the occurrence of peak temperature and the subsequent cooling during the forging phase. The axial temperature distribution is also well reproduced, with the highest temperatures and steepest gradients at the weld interface, followed by a gradual decrease of the temperature with increasing distance from the interface.

Despite these qualitative agreements, significant deviations in the absolute temperatures were observed. At the weld interface (TC2), the predicted peak temperature is in good agreement with the experimental measurement, indicating that the overall magnitude of interfacial heat generation is reasonably captured by the numerical model. However, the simulated cooling rate is higher than that was observed in the experiment, suggesting an overestimation of heat dissipation from the interface region. The model underpredicts the peak temperatures, at other TCs particularly at TC4, TC10 and TC6, while predictions improve at locations farther from the interface at TC12 and TC8. The overall cooling trends were captured reasonably well. The underestimation of these temperature indicates that, although the current numerical model replicates the heat generation at the interface, it has not yet been fully calibrated. This is likely due to the assumptions in the interfacial friction coefficient and higher heat transfer coefficients which are difficult or impossible to measure. The experimental temperature data therefore provide a critical basis for the further refinement and calibration of the numerical model.

The comparison of flash geometries, as illustrated in Fig. 10(b), reveals that the experimentally obtained flash exhibits a stronger curvature and wraps back towards the aluminium component. In contrast, the simulated flash has a larger radius of curvature and does not fully close to the aluminium. Insufficient interface temperatures in the simulation results in higher flow stresses in the aluminium. This means that less material is displaced during the friction phase, resulting in reduced curvature in the flash. During the forging phase, the material flows more strongly in radial direction. This further supports the conclusion of uncertainties in the heat transfer coefficients including heat conduction to the aluminium component, heat partitioning at the interface and heat losses to the surroundings.

While the current model captures the main flow mechanisms and fundamental thermo-mechanical trends of RFW, quantitative agreement requires further refinement of the interfacial heat generation parameters and energy localization. In particular, using temperature data from the steel specimen to predict the flash geometry of aluminium remains challenging due to complex heat conduction and heat transfer at the dissimilar interface. The agreement between experiment and simulation confirms that the developed numerical model, implemented using a user-defined subroutine, provides a valid proof of concept for predicting temperature evolution and flash formation in dissimilar RFW.

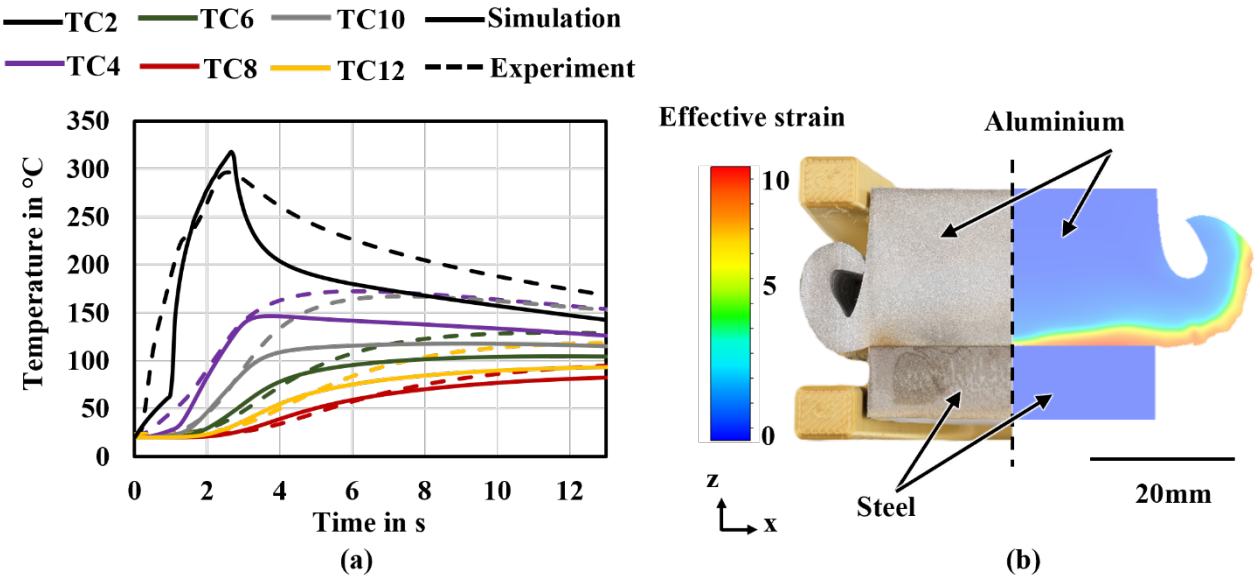

Fig. 10. (a) Temperature evolution for experimental PC 11 compared with numerical predictions; (b) corresponding comparison of flash geometries, illustrating differences in curvature and material flow between experiment and simulation.

Summary and Outlook

An experimental study of RFW between 20MnCr5 and EN AW-6082 was performed to investigate the influence of process parameters on temperature evolution, plastic deformation and flash formation. The results indicate that rotational speed is the dominant factor controlling frictional heat generation, peak temperature and plastic flow, whereas friction pressure primarily affects plastic deformation with a limited influence on the peak temperature. The sledge path during the friction phase was found to be a reliable indicator of material softening and flash formation. In-situ temperature measurements in the steel specimen provided stable and reproducible thermal data, serving as a robust basis for numerical model calibration. Overall, this study demonstrates the key thermo-mechanical mechanisms governing steel–aluminium RFW and establishes a solid experimental foundation for future numerical modelling and process optimization of dissimilar metal joints.

The numerical simulations qualitatively reproduced the dominant trends in temperature, including peaks and axial distribution, as well as key features of flash morphology, such as curvature and material flow patterns. Quantitative deviations were observed, with the model predicting lower peak temperatures, higher cooling rates at the interface and thus predicting lower material flow. This highlights the importance of accurately modelling interfacial friction and heat transfer conditions. Overall, the combined experimental and numerical study demonstrates the fundamental thermo-mechanical mechanisms governing RFW and provides a platform for future model enhancement. The numerical model can be further developed to improve quantitative accuracy and readily extended to incorporate intermetallic formation behaviour, offering a predictive tool for a wide range of dissimilar metal joints.

Acknowledgements

Funded by the Deutsche Forschungsgemeinschaft (DFG, German Research Foundation) – 252662854 - SFB 1153, subprojects A01 and B03.

References

[1] X. Sun, F. Meng, J. Liu, J. McKechnie, J. Yang, Life cycle energy use and greenhouse gas emission of lightweight vehicle – a body-in-white design, Journal of Cleaner Production 220 (2019) 1–8. https://doi.org/10.1016/j.jclepro.2019.01.225

[2] A. Mayyas, M. Omar, M. Hayajneh, A.R. Mayyas, Vehicle's lightweight design vs. electrification from life cycle assessment perspective, Journal of Cleaner Production 167 (2017) 687–701. https://doi.org/10.1016/j.jclepro.2017.06.249

[3] L. Huber, P. Schultheiß, M. Thiele, C. Rößler, H.W. Höppel, Impact of Various Rotary Friction Welding Process Parameters on the Mechanical Properties of a Steel–Aluminum Joint, Advanced Engineering Materials (2025) e202500842. https://doi.org/10.1002/adem.202500842

[4] B.-A. Behrens, J. Uhe, Introduction to tailored forming, Production Engineering: Research and Development 15 (2021) 133–136. https://doi.org/10.1007/s11740-021-01050-9

[5] A. Gullino, P. Matteis, F. D'Aiuto, Review of Aluminum-To-Steel Welding Technologies for Car-Body Applications, Metals 9 (2019) 315. https://doi.org/10.3390/met9030315

[6] S. Senthil Murugan, P. Sathiya, A. Noorul Haq, Rotary Friction Welding and Dissimilar Metal Joining of Aluminium and Stainless Steel Alloys, Annals of "Dunărea de Jos" University of Galați, Fascicle XII: Welding Equipment and Technology 32 (2021) 85–92. https://doi.org/10.35219/awet.2021.11

[7] P. Lacki, J. Adamus, W. Więckowski, M. Motyka, A New Method of Predicting the Parameters of the Rotational Friction Welding Process Based on the Determination of the Frictional Heat Transfer in Ti Grade 2/AA 5005 Joints, Materials 16 (2023) 4787. https://doi.org/10.3390/ma16134787

[8] N. Mohnfeld, H. Wester, G. Tunc Karaer, A. Piwek, J. Uhe, Numerical investigation of rotational friction welding for C22.8–41Cr4 joints using a substitute model, in: A.C. Araujo, A. Cantarel, F. Chabert, A. Korycki, P. Olivier, F. Schmidt (Eds.), Material Forming – ESAFORM 2024, Materials Research Proceedings 41 (2024) 1668–1677. https://doi.org/10.21741/9781644903131-185

[9] C.-A. Li, G. Qin, B. Fu, B. Yang, H. Wang, C. Zhang, J. Zhou, Z. Zhang, Simulation of interfacial friction regime transition in inertia friction welding, International Journal of Mechanical Sciences 303 (2025) 110643. https://doi.org/10.1016/j.ijmecsci.2025.110643

[10] M. Winkler, C. Rößler, N. Harriehausen, S. Jüttner, D. Schmicker, F. Trommer, An energetic approach to the statistical analysis and optimization of friction welding processes applied to an aluminum-steel-joint, Journal of Advanced Joining Processes 10 (2024) 100251. https://doi.org/10.1016/j.jajp.2024.100251

[11] L. Wang, M. Preuss, P.J. Withers, G. Baxter, P. Wilson, Energy-input-based finite-element process modeling of inertia welding, Metallurgical and Materials Transactions B 36 (2005) 513–523. https://doi.org/10.1007/s11663-005-0043-y

[12] M. Yılmaz, M. Çöl, M. Acet, Interface properties of aluminum/steel friction-welded components, Materials Characterization 49 (2002) 421–429. https://doi.org/10.1016/S1044-5803(03)00051-2

[13] H. Ghari, A. Taherizadeh, B. Sadeghian, B. Sadeghi, P. Cavaliere, Metallurgical characteristics of aluminum-steel joints manufactured by rotary friction welding: A review and statistical analysis, Journal of Materials Research and Technology 30 (2024) 2520–2550. https://doi.org/10.1016/j.jmrt.2024.03.089

[14] C. Bennett, Finite element modelling of the inertia friction welding of a CrMoV alloy steel including the effects of solid-state phase transformations, Journal of Manufacturing Processes 18 (2015) 84–91. https://doi.org/10.1016/j.jmapro.2015.01.003

[15] H. Mani, A. Taherizadeh, B. Sadeghian, B. Sadeghi, P. Cavaliere, Thermal–Mechanical and Microstructural Simulation of Rotary Friction Welding Processes by Using Finite Element Method, Materials 17 (2024) 815. https://doi.org/10.3390/ma17040815

[16] K.W.P. Nagappan, K. Wang, Transient temperature distribution in inertia welding of steels, Welding Journal 49 (1970) 419–426.

[17] A. Moal, E. Massoni, Finite element simulation of the inertia welding of two similar parts, Engineering Computations 12 (1995) 497–512. https://doi.org/10.1108/02644409510799730

[18] K. Lee, A. Samant, W.T. Wu, S. Srivatsa, Finite element modeling of inertia welding processes, in: K.-I. Mori (Ed.), Simulation of Materials Processing: Theory, Methods and Applications (Proceedings of the International Conference on Numerical Simulation of Materials Processing, NUMIFORM 2001), A.A. Balkema, Lisse, 2001, pp. 1095–1100.

[19] L. D'Alvise, E. Massoni, S.J. Walløe, Finite element modelling of the inertia friction welding process between dissimilar materials, Journal of Materials Processing Technology 125–126 (2002) 387–391. https://doi.org/10.1016/S0924-0136(02)00349-7

[20] B.-A. Behrens, J. Uhe, T. Petersen, F. Nürnberger, C. Kahra, I. Ross, R. Laeger, Contact Geometry Modification of Friction-Welded Semi-Finished Products to Improve the Bonding of Hybrid Components, Metals 11 (2021) 115. https://doi.org/10.3390/met11010115

[21] H. Wester, B.-A. Behrens, Numerical Process Analysis of Forming Semi-Finished Hybrid Parts, Key Engineering Materials 957 (2023) 135–142. https://doi.org/10.4028/p-p1hZbB

[22] A. Dewidar, A. Verschinin, N. Mohnfeld, H. Wester, S. Barton, H.J. Maier, J. Uhe, Experimental investigation of rotational friction welding for EN AW-6082–20MnCr5 joints, in: Material Forming – ESAFORM 2025, Materials Research Proceedings 54 (2025) 1479–1488. https://doi.org/10.21741/9781644903599-160

[23] B. Lei, Q. Shi, L. Yang, C. Liu, J. Pan, G. Chen, Evolution of interfacial contact during low pressure rotary friction welding: A finite element analysis, Journal of Manufacturing Processes 56 (2020) 643–655. https://doi.org/10.1016/j.jmapro.2020.05.034

The publication of this article was funded by the Leibniz Universität Hannover (LUH) / Technische Informationsbibliothek (TIB)